High-rate accumulation of tiny aqueous droplets using a pyro-electrohydrodynamic jet system

Volodymyr Tkachenko*, Reinhard Schwödiauer, Romina Rega, Simona Itri, Martina Mugnano, Danila del Giudice, Heidi Ottevaere, Yunfeng Nie, Pietro Ferraro, Simonetta Grilli

Dr. V. Tkachenko, Dr. R. Rega, Dr. M. Mugnano, Dr. P. Ferraro, Dr. S. Grilli
Institute of Applied Sciences and Intelligent Systems (ISASI), National Research Council of Italy (CNR), 80078, Pozzuoli (NA), Italy
E-mail: v.tkachenko@isasi.cnr.it

S. Itri, D. del Giudice
Institute of Applied Sciences and Intelligent Systems (ISASI), National Research Council of Italy (CNR), 80078, Pozzuoli (NA), Italy;
Department of Mathematics and Physics, University of Campania, 81100 Caserta, Italy

Dr. Reinhard Schwödiauer
Johannes Kepler University, Altenbergerstraße 69, 4020 Linz, Austria

Prof. Dr. Ir. Heidi Ottevaere, Dr. Yunfeng Nie
Vrije Universiteit Brussel and Flanders Make, Brussel Photonics, Dept. of Applied Physics and Photonics, Pleinlaan 2, 1050 Brussel, Belgium

It is well known how the quantification of tiny amounts of molecular species in biological assays is a crucial issue. We present here a deep investigation on a pyro-electrohydrodynamic jet system at aim to demonstrate its capability to accumulate with high efficiency a large number of tiny aqueous droplets on the surface of a target slide. It makes use of the pyroelectric effect in a lithium niobate crystal for producing a continuous jetting of tiny droplets, thus reducing drastically the volume of sample required for successive biochemical reactions. The nozzle-free nature of this approach allows us to obtain tiny droplets avoiding cross contamination with mixing buffers usually employed for modulating the surface tension

of the liquid. We characterize the performance of the system in terms of electrical field and crystal size experimentally as well as numerically. An optimal condition was found that produce deposition of more than 100 picoliter-sized droplets in 14 seconds. Thus, we estimate a possible 70-fold increase of the analyte concentration in the overlap region with a diameter of less than 40 microns, compared to an individual droplet deposition. Moreover, in case, an additional increase can be achieved simply by extending the droplet accumulation time. This approach may find application in all of those crucial biological assays where highly diluted analytes could be detected by increasing the density of molecules per unit area and hence reducing the volume of reaction.

1. Introduction

The demand on sensitivity improvement beyond the common limit of detection (LOD) of about 1 pM is always of increasing importance for the detection of biomolecules in highly diluted solutions.[1,2] Moreover, the increasing need for more rapid and non-invasive assays in biomedicine requires the search for biomolecular markers in peripheral body fluids (e.g. saliva; capillary blood; tears) where their concentration is highly diluted and the available volumes are reduced. Just as an example, in case of the Alzheimer's disease a non-invasive diagnosis that avoids the withdrawal of cerebrospinal fluid is still highly desired.[3] One way to proceed involves the development of techniques able to amplify the number of molecules while another family of strategies regard the ability of reducing the reaction volume in order to increase the analyte concentration, leading to an amplification of the signal.[4] For example, Giordano et al. used a microfluidic-based platform for performing an oil-assisted water extraction in trapped microwells, while other groups have presented a polarization-based phenomenon.[6-8] Alternatively, a sessile drop evaporating on a superhydrophobic structure

2

or in presence of Marangoni flow inside can be used for increasing the analyte concentration.[9-11] However, microfluidics-based methods need rather large volumes of sample while the methods with sessile drops require the use of challenging techniques for the fabrication of the substrate. Moreover, the employment of oil-based mixing buffers can be highly detrimental for the chemical-physical stability of the biological samples.

Recently, we demonstrated how the pyroelectric effect in lithium niobate (LN) crystals can be used for generating high electric fields in the order of a few kV/mm through an innovative electrode-free configuration. These fields were used for ejecting tiny daughter droplets from the free meniscus of a mother drop with a sub-μL volume.[12-15] We called it pyro-electrohydrodynamic jet (p-jet) and we demonstrated its usefulness for accumulating protein-based as well as sugar-based molecules, by printing multiple overlapping droplets on a restricted area.[16-18] The key advantage of the p-jet is to be nozzle-free, thus allowing us to avoid the typical clogging drawbacks encountered in conventional inkjet printers.

Here we present a significant step forward in which we produce a much higher number of aqueous tiny droplets in a single thermal stimulation, by applying an appropriate heating ramp on a small piece of LN crystal thus achieving good control of the jetting operation. A quasi-static pyroelectric field is generated that slowly decays due to the attraction of charges from the environment to the crystal surface. The decay of the electric field governs the duration of the p-jet, and therefore being the important feature of the droplet accumulation process. Here we study this decay experimentally as a function of the LN crystal size. In addition, the influence of the crystal size LN on the distribution of the electric field around the upper surface of the crystal and the meniscus was investigated numerically. We use here a top-down configuration of the p-jet system in which a micro-orifice allows us to load a higher volume of sample, thus being free from the crucial deposition of the sample in the

form of a sub-μL mother drop, as occurred in the previous bottom-up arrangements.[14,17-19] Finally, we demonstrate the ability of the proposed p-jet configuration to accumulate about 70% of the dispensed aqueous droplets into a limited area with a micrometric cross size, thus opening the perspective for a more affordable concentrator of analytes in aqueous solutions.

2. Results and discussion

2.1. Pyro-electrohydrodynamic jet system

Figure 1a shows the schematic view of the top-down configuration of the p-jet used here for achieving a high-rate accumulation of tiny aqueous droplets ejected from the liquid's meniscus.
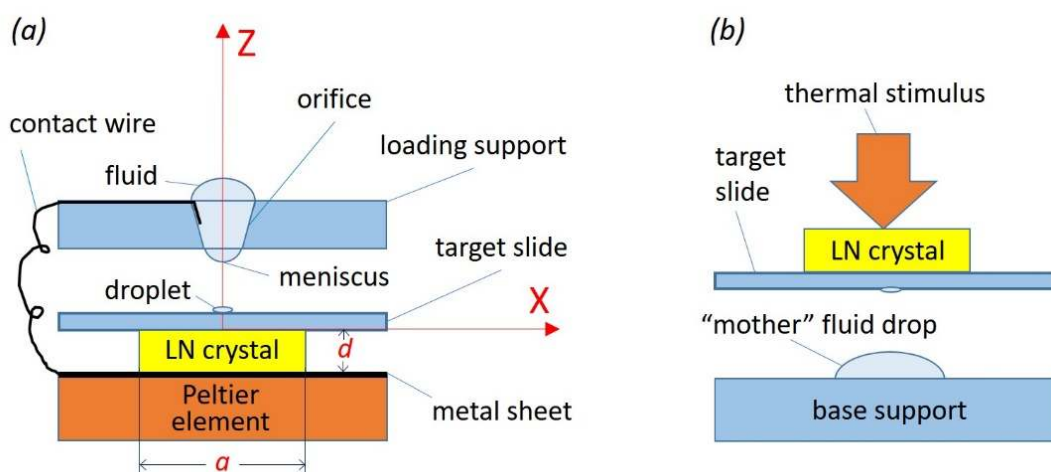
Figure 1. a) Schematic view of the top-down p-jet configuration where the *XZ* coordinates and the crystal dimensions refer to the simulation model indicated later. b) Schematic view of the bottom-up p-jet configuration used in our previous papers as a comparison.

The aqueous sample (around 10 μL) is loaded manually by a standard pipette into the micro-orifice of an innovative slide that we call here "loading support". See the Supporting Information for more details. Once the micro-orifice is filled with the sample liquid, a stable meniscus emerges as described in the Supporting Information. A standard XYZ micrometric

manual translation stage is used for aligning the micro-orifice aperture with the central point

of a square piece of LN crystal, which size is described later. LN is a pyroelectric material,

meaning that is able to generate a non-negligible surface potential upon an appropriate

variation of its temperature (see Methods for details). The target slide, namely the slide

where accumulating the tiny droplets, is a commercial SuperAmine 2 slide usually used for

binding biomolecules (SMM2, ArrayIt®) and is inserted between the orifice and the LN crystal.

The slide is 75x25 mm^2 sized and 1 mm thick. The heating element underneath the crystal

belongs to a commercial heating plate (Linkam) or to a standard Peltier element 15x15 mm^2

sized (see Methods for details). As described in Methods, a thin metal wire is inserted into

the orifice, which put in contact the liquid and a thin metal sheet between the crystal and the

heating element, in order to ensure electrical neutralization of the meniscus after emission

of a charged droplet and to enhance the electric field strength.

It is important to note the step forward developed here compared to our previous papers

where we used a bottom-up configuration (see Figure 1b). Two options were used there for

the thermal stimulation: (1) CO_2 laser radiation and (2) Joule effect from a titanium coil

integrated on the back face of the crystal.[16-19] The laser-based system was extremely bulky,

while the coil-based heater needed expensive and time-consuming microfabrication. The

common disadvantage was the need for a sub-µL mother drop in order to produce tiny

droplets, thus producing a reduced number of ejected droplets in a single thermal

stimulation.

2.2. Simulation of the electric field

Prior the application of the p-jet for dispensing tiny droplets, here we simulated numerically

the spatial distribution of the electric field E generated by considering a fixed temperature

variation ΔT=15 K for different crystal sizes, in order to find the best conditions for achieving the high-rate droplet ejection. The fairly small value of ΔT was chosen keeping in mind the potential use of this set-up for accumulating biomolecules, and thus avoiding conditions that may cause their thermal damage.

The surface of the meniscus is taken to be spherical with a radius of 0.4 mm in accordance with the side view images experimentally recorded with a CMOS camera (see the Supplementary video 1). The meniscus must have the same electrical potential as the contact wire that is electrically connected to the backside of the LN crystal (see Figure 1a), keeping in mind that the electrical relaxation time of the aqueous sample is much shorter than the characteristic time of all other involved processes.[20] We focused our attention on two values of the crystal thickness d (0.5 mm and 1 mm) and on four values of the side length a (2 mm, 6 mm, 10 mm, 14 mm). For these simulations we refer to the coordinates indicated in Figure 1a and we studied the distribution of E strength first at X=0 (centre of the crystal) along the Z axis, and secondly at Z=0.01 mm, namely close to the surface of the crystal, along the X axis from 0 (centre of the crystal) up to the edge of the crystal. See Methods for details about the simulation procedures.

Figure 2a presents the E distribution along the Z axis at X=0. Here Z=1 mm and Z=1.37 mm correspond, respectively, to the upper surface of the target slide, namely the surface where the droplets are accumulated, and to the apex of the liquid meniscus pending from the orifice (see the scheme in Figure 1a). The field strength increases significantly in the vicinity of the meniscus, as is usually the case near a strongly curved conductive surface. Moreover, it increases with increasing the crystal side length but the field increment is negligible at $a{\geq}6$ mm. Thicker crystals (d=1 mm, red lines) always generate fields about twice that of thinner crystals (d=0.5 mm, black lines). That is in agreement with the fact that electric potential

difference between +*z* and −*z* surfaces of a pyroelectric crystal is proportional to the crystal thickness (see Methods).
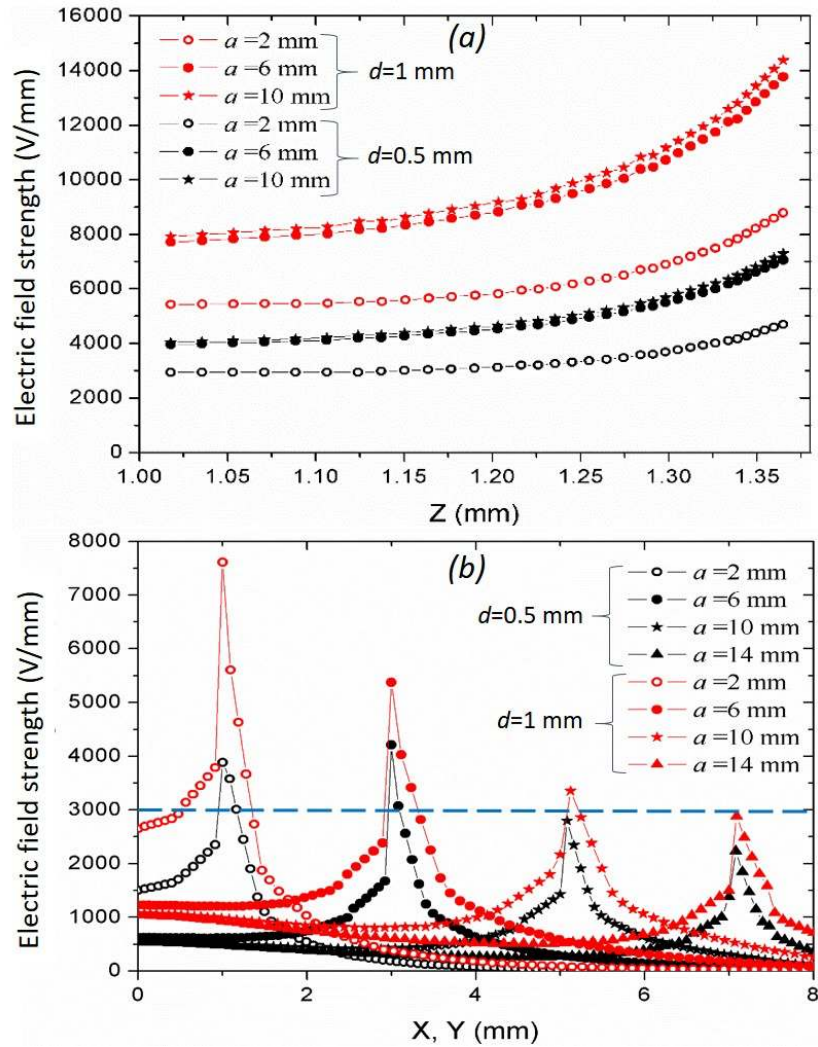
Figure 2. a) Simulated *E* field strength along the *Z* axis at *X*=0 for side length of 2, 6, and 10 mm. b) Simulated *E* field strength along the *X* axis at *Z*=0.01 mm (close to the crystal surface) for side length of 2, 6, 10, and 14 mm. The blue horizontal line corresponds to the typical value of the electric breakdown threshold in air under normal laboratory conditions. The black and red lines correspond to *d*=0.5 mm and *d*=1 mm, respectively.

Figure 2b shows the results for the *E* distributions along the *X* or *Y* axis (note that two axes are equivalent due to problem symmetry) for *Z*=0.01 mm. First of all, the spiking effect of the electric field is clearly evident in correspondence of the edge of the crystal for all *d* and *a*, with

7

E values ranging from about 2.3 kV mm^{-1}, in case of *d*=0.5mm and *a*=14mm, up to about 7.7 kV mm^{-1} in case of *d*=1mm and *a*=2mm. This suggests to use the central region over the crystal as source for the electric field, namely at *X*=*Y*=0, in order to avoid the highly inhomogeneous field. The blue horizontal line corresponds to the typical value of the electrical breakdown threshold in air under normal laboratory conditions (about 3 kV mm^{-1}). Thereby, Figure 2b clearly demonstrates that *E* values overcome an electric breakdown threshold at the edges of the LN plate with *a*≤6 mm and *a*≤10 mm for the thin and thick crystal, respectively. The intense generation of ions due to a corona discharge and their accumulation on the crystal surface is expected here resulting in pyroelectric potential decay.[21] It is reasonable to assume that the rate of ion generation increases with an increase in the area of the crystal, on which an electrical breakdown occurs. Figure 2b demonstrates that this area enlarges with the plate side length decreasing and thickness increasing. On the other hand, the amount of accumulated external charges required for a noticeable drop in the pyroelectric potential should be proportional to the crystal surface area. As a result, the characteristic decay time is expected to increase with increasing surface and decreasing thickness of the crystal plate. We investigated experimentally this decay time as a function of crystal size. The corresponding results will be presented and discussed in the next section.

In summary, the simulations along *Z*-axis demonstrate that the highest *E* is achieved by using the thicker crystal (*d*=1mm) and side length *a*=6mm, with a negligible difference for increasing *a*. These results are consistent with the simulation results along the *X*-axis that identify with *a*≥6 mm the side length which can provide a sufficiently long p-jet process. Therefore, the overall simulations performed in this section demonstrate that we have to focus our attention on crystal samples with side length *a*≥6 mm.

2.3. Measurement of electric potential decay

We changed the temperature of the pyroelectric crystal by 15 K, as in case of the simulations, with the aim at identifying the crystal size that produces the potential as much stable as possible over time, and hence able to produce the higher number of tiny droplets in a single thermal stimulation. The potential was measured as a function of time t for samples LN of two thicknesses d=0.5 mm and d=1 mm with a side length, $a,$ of 1.6, 2.6, 3.6, 7.6, 8.6 and 16 mm. The crystal dimensions are specified as in Figure 1a. The measurements were carried out in an ambient atmosphere at 25 ° C and 24% relative humidity.

Figure 3a shows the schematic view of the equipment used for the pyroelectric potential measurements. We used a commercial Linkam system to control the LN crystal temperature with the time dependence shown in Figure 3b. The temperature was increased from the room value of 25°C up to T=40°C during the time interval from t=15 s to t=45 s and from t=17 s to t=27 s for the crystals with d=0.5 mm and d=1.0 mm, respectively. After that, the temperature was kept constant (see Methods for details). It is important to note that the diameter of the heating element was 22 mm, which made it possible to cover the entire crystal surface for all values of a studied here. The potential was measured through a commercial Kelvin probe at a distance Z=1.5 mm from the surface of the crystals (see Methods for details). Figure 3c and 3d show the results in case of fixed thickness d=0.5 mm and d=1 mm, respectively, and for different values of the side length a.
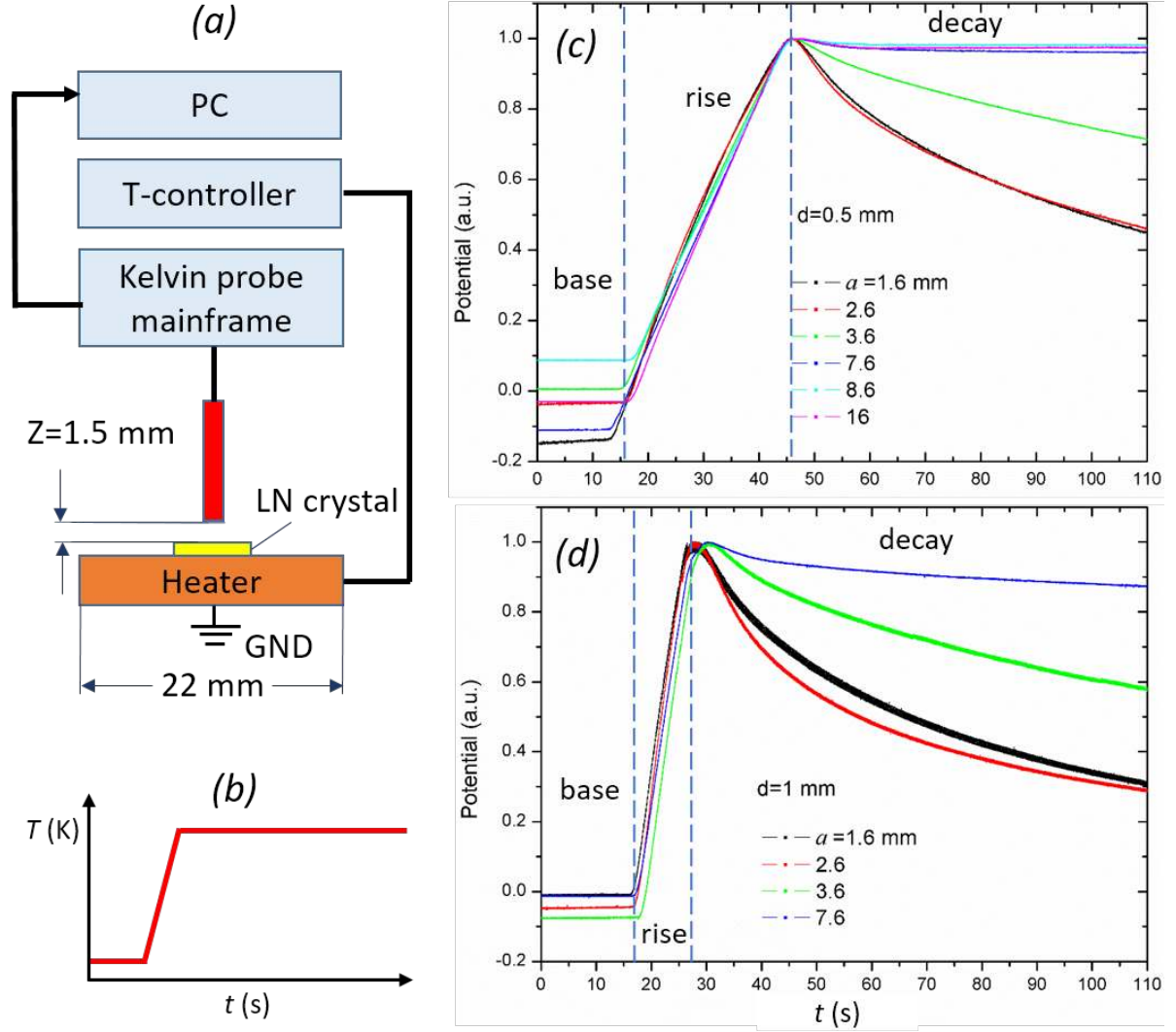
Figure 3. a) Schematic view of the set-up used for measuring the electrical potential generated by the LN crystal under a step-wise temperature variation. b) Shape of the crystal temperature dependence on time. c,d) Temporal behavior of the electrical potential for the crystals with thickness d=0.5mm and d=1mm, respectively. The crystal side length a takes discrete values from 1.6 to 16 mm. The dashed blue lines separate the "base", "rise" and "decay" regions.

The electric potential was in the range from 1 to 2.5 kV for crystals with a thickness of 0.5 mm, while it could exceed 4.5 kV for crystals with a thickness of 1 mm and a>7.6 mm resulting in an electrical breakdown between the crystal surfaces. Therefore, in the latter case, we limited ourselves to a crystal side length of 7.6 mm. Note that the absolute value of the electric potential can be measured with a rather high error, especially for small LN samples,

but it is not important because here we are focused on the relative change in potential over time.[22] The curve of the electrical potential exhibits three main regions in all cases, that we call here "base", "rise" and "decay", as indicated by the labels in Figure 3c and 3d. The base corresponds to the initial potential, the rise to potential growth during the linear T increase and the decay region starts when the T value is kept constant. It is worth noting that each a value corresponds to a different sample and therefore the base of the potential curve appears slightly different for each value of a, due to the different pre-existing charge accumulation.

For both values of thickness, the decay accelerates significantly with decreasing a, exhibiting three main rates that we call "fast", "medium" and "slow". The fast rate includes the crystals with a=1.6 mm (black lines) and a=2.6 mm (red lines), with negligible differences, while the medium region regards the crystal with a=3.6 mm (green lines). Finally, the slowest decay is achieved for crystals with $a{\geq}7.6$ mm, with negligible differences for increasing length. In particular, the data shown in Figure 3c and 3d show, respectively, that 55 s (graph d=0.5 mm) and 40 s (graph d=1 mm) after reaching the peak value the potential decays by only 5% in case of larger samples ($a{\geq}7.6$ mm), with almost constant value later, while reduces by about 20% in case of the shorter side length (a=1.6 mm and a=2.6mm) with subsequent further decline over time. These measurements show that a crystal with a side length of more than 8 mm provides a fairly stable electrical potential over time.

It is well known that the electrical potential decays gradually over time due to three main factors: i) bulk conductive current; ii) ferroelectric electron emission; iii) accumulation of screening charges from the ambient atmosphere on the crystal surface.[21,23] Here the screening from electron emission is negligible because the crystal is exposed to the normal atmosphere, while the bulk conductive screening occurs very slowly with a relaxation time around 10^5-10^7 s.[23] Therefore, we believe that the temporal decay of the electric potential

over tens or hundreds of seconds is mostly related to the charge recombination on the surface of the crystal through the ambient ions produced by the electric breakdown along the edges of the crystal, i.e. where the breakdown threshold is overcome.[23] Crystals with a longer side and, therefore, a larger surface (see the curves for a>3.6 mm in Figure 3c) exhibit slow decay, since a smaller surface fraction is covered by screening charges during the same time interval compared to crystals with smaller surface. Among crystals with the same side length, thicker crystals exhibit faster decay as they create a higher electric field at the edges, thereby accelerating the formation of ions in the environment (compare green or blue lines in Figure 3c and 3d). We can conclude that the experimental results are consistent with expectations based on electric field simulations. However, it is important to note that this study allowed us to find an optimal condition in which electrical potential is stable over time.

2.4. High-rate accumulation of aqueous droplets

Taking into account the simulation of the electric field and the measurement of the electric potential, we configured the p-jet setup schematically shown in Figure 1a using a crystal sample 1 mm thick and 7 mm side length, which was expected to provide an electric field sufficiently high and stable for several tens of seconds. We loaded about 10 μL of distilled water in the orifice and we positioned the lower face of the loading support at about 300 μm from the top surface of the target slide. The Peltier element was 15x15 mm² large and was driven by a step-wise current pulse of 0.5 A (with 0.6 V voltage) provided by a programmed power supply HCS-3300, in order to raise the crystal temperature from 25°C up to about 40°C.

The Supplementary Movie 1 shows the side view of the typical high-rate droplet ejection occurring here. These images were recorded at 50 fps frame rate by using a conventional optical system comprising an illuminating LED source, a microscope objective and a PC

controlled camera, which has been described elsewhere.[17] The images show a continuous deposition of the aqueous droplets drawn from the orifice on the surface of the target slide. The droplet ejection starts 7 s after Peltier power on and finishes after about 46 s, when the electric field decreases to an electrohydrodynamic (EHD) jetting threshold due to screening charges accumulated on the crystal surface.[24] All droplets are deposited within a target slide area with a diameter of about 150 μm.

We analysed the images of the recorded movie in order to evaluate quantitatively the rate of accumulation of the droplets on the target slide. The video frames in the first 14 seconds were cropped to the region of interest with a width of 500 pixels and a height of 100 pixels, taking into account that the pixel size of the images was about 0.6 μm, and the first frame was used as a reference to be subtracted from the others to remove the background (see the Supplementary Movie 2). We used here a transmission-based illumination of the water jets and, therefore, the dark pixels in the frame corresponded to the region where there was liquid attenuating the light from the LED source. The contour of that dark pixel area outlined a side view of the deposited water drop together with its reflection in the target slide and so it was used for measurements of various geometrical parameters of the drop such as their height above the target slide, diameter of a base, and deposition coordinate. Other parameters such as a contact angle and a drop volume were calculated from the measured ones (see the Supporting Information for details).

The contact angle of 74° was obtained by averaging over the all cases of droplet deposition. The volume was slightly different for each droplet and it is well known that the evaporation rate decreases with increasing volume. Hence, for some jet events, we had an overlapping of a droplet on the previous one, when not evaporated completely. Therefore, in order to quantify each droplet volume as best as possible, we subtracted the volume of the deposited

13

liquid at the frame preceding to the jet event, in order to remove the contribution from the previous droplet not evaporated completely. The events of droplet deposition are illustrated by **Figure 4** which present the frames extracted from the Supplementary Movie 1. Figure 4b and 4d correspond to the deposition of the first and second droplets, and Figure 4a and 4c - frames preceding these events, respectively. Figure 4e shows all deposition events of individual droplets versus time, represented by peaks with a height equal to the droplet volume V, expressed in picoliters. The figure demonstrates that we identified 92 jets of individual droplet within approximately 14 seconds, while 14 multiple (2-3) droplet ejection events were excluded from the analysis. A time interval between two adjacent jetting events ranges from 0.10 to 0.66 s. Note that typically EHD droplet jetting is non-periodic for low liquid flow rates, in agreement with Ref. [24]. Droplet volumes range from 5 to 25 pl with an average of 14 pl and a standard deviation of 4.8 pl.
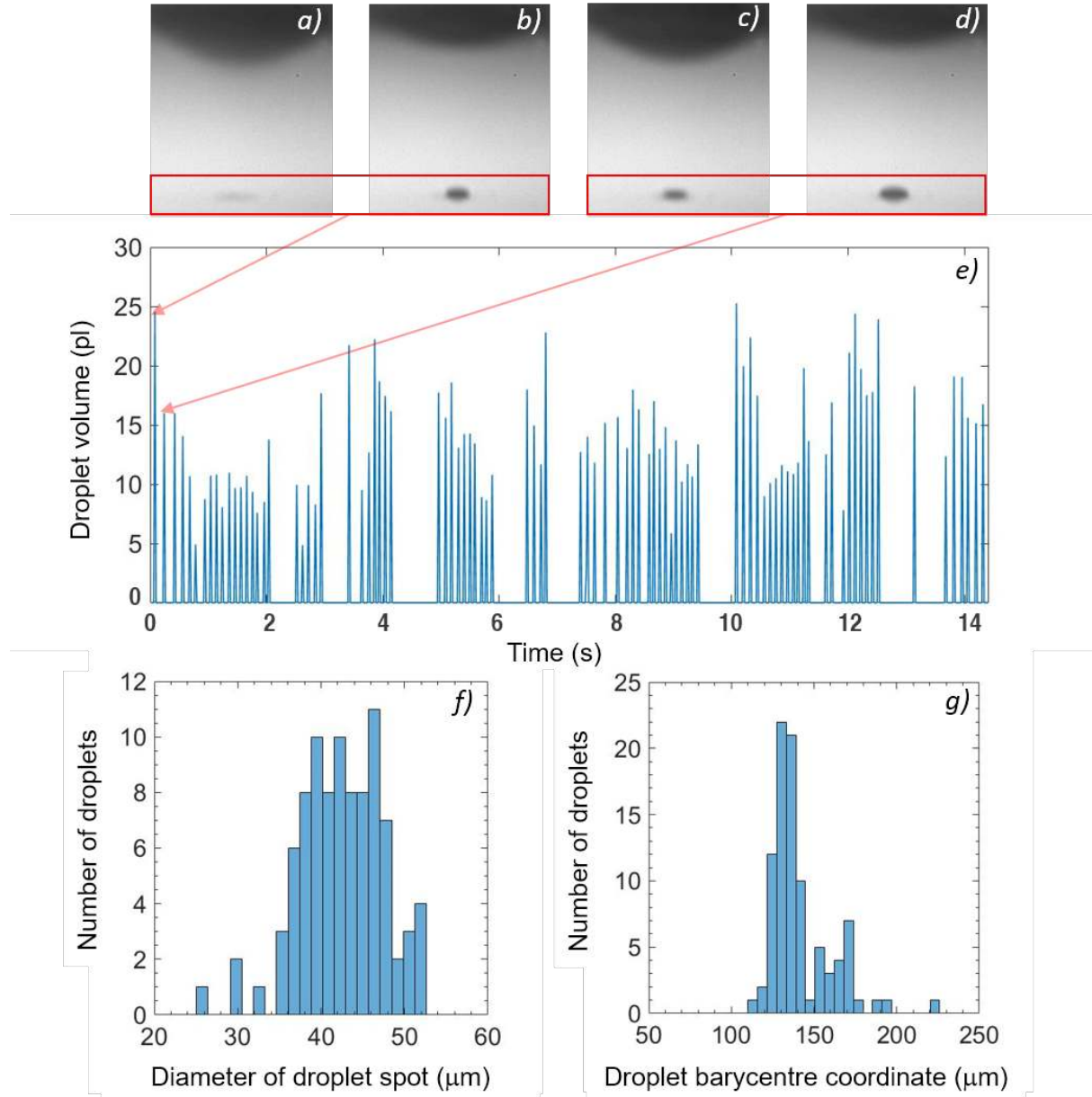
Figure 4. b,d) Frames from Supplementary Movie 1 corresponding to deposition events of the first and second droplets, respectively. a,c) Frames preceding these events, respectively. e) Droplet deposition events as a function of time, represented by peaks with a height equal to the droplet volume, where the red arrows indicate the first and second droplet deposition events. f) Histogram for the distribution of a diameter of the area which can be covered by the individual droplet. g) Histogram for the distribution of the droplet barycentre coordinate.

The following analysis aims to estimate how many droplets overlap on the restricted area of a target slide. To this end, we calculated the diameter of the area that each ejected droplet

with a known volume V can cover and the X coordinate of its deposition (see the Supporting Information for details).

The diameter of the covered area (here we call this area a "droplet spot" for brevity) was calculated on the assumption that a deposited droplet has a 74 ° contact angle with the target slide surface and forms a spherical interface with air. The histogram in Figure 4f shows the frequency distribution for a droplet spot diameter. The mean value of a droplet spot diameter D_{mean} is 42.5 μm.

To calculate the barycentre coordinate of the deposited droplet we retrieved a series of images (see the Supplementary Movie 3) obtained by subtracting the previous frame from each frame of the Supplementary Movie 2. Here the dark pixels, which correspond to the contribution of the previous droplet not evaporated completely, are excluded from the image of the deposited droplet. Then we found a barycentre coordinate of the deposited droplets using a standard procedure integrating the grey levels of the pixels. The histogram of the frequency distribution of the barycentre coordinate is plotted in Figure 4g. The histogram demonstrates that 74 droplets have the barycentre coordinate in a region about 40.6 μm wide, which is less than D_{mean}, and so the droplet spots overlap at least partially within this region. This can provide an approximately 70-fold increase in the surface density of the analyte molecules dissolved in the aqueous sample compared to the deposition of a single drop. It is noteworthy that, firstly, this increase is underestimated since we excluded the jets with multiple droplets, and secondly: the surface density of molecules can be enhanced simply by increasing the accumulation time of the droplets.

In conclusion, we developed here a new p-jet configuration able to produce a quasi-static pyroelectric field which allows us to achieve high-rate accumulation of tiny aqueous droplets in a single thermal stimulation. The key feature relies on the Peltier-based heater element,

16

able to apply a single rise temperature onto a small piece of LN crystal. We optimized the LN crystal thickness and side length in order to produce pyroelectric field sufficient for EHD droplet dispensing during time interval of about 40 seconds. The experimental results demonstrate accumulation of more than 70 tiny aqueous droplets during the first 14 seconds on the target area with a diameter of less than 40 μm. We believe that this technique could open the route to easy accumulation of biomolecules for high-sensitive detection of highly diluted biomarkers.

3. Methods

Lithium niobate crystals: Both sides polished and z-cut wafers of monodomain LN with 0.5 mm thickness and 3-inch-diameter were bought from Crystal Technology Inc. The wafers were cut into square samples with a side length of 1.6, 2.6, 3.6, 5.0, 7.6, 8.6, and 16 mm by a standard precision diamond saw. To obtain LN samples with a thickness of 1 mm, two cleaned LN plates with a thickness of 0.5 mm with the same lateral dimensions and polarization direction were stacked up and glued together with standard thermal paste. The spontaneous polarization P_s of the LN crystal changes according to $\Delta P_s = p \, \Delta T$, where p is the pyroelectric coefficient and ΔT is the temperature variation (p=−8.3 × 10^{-5} C m^{-2} K^{-1} at T=298 K). At thermal equilibrium the spontaneous polarization of the crystal is completely screened by the external charges accumulated on the crystal surfaces and no electric field is present.[21] When the crystal is stimulated through a temperature variation, an uncompensated surface charge density $\sigma = \Delta P_s$ and electric potential difference $\Delta U \sim \sigma d / _{\varepsilon_0 \varepsilon}$ appears on the crystal surfaces (here d is crystal thickness and ε_0 and ε are dielectric constants of vacuum and of the crystal, respectively). This potential difference can reach 10^4 V for mm-sized crystal thickness and ΔT of about 10 K.

Heating element: The crystal plate was mounted with silicone thermal grease from RS on top of a heater. We used two kinds of heater which were able to heat LN plate homogeneously over its largest surface. The first one is HFSX350 heating-freezing stage from Linkam Scientific Instruments. It has a disk-shaped heating/cooling element with a diameter of 22 mm and is able to provide heating rate up to 90°C per minute and to keep preselected temperature of the element with precision of 0.1°C. The second one is based on the commercial Peltier element from Laird with lateral dimensions of 15x15 mm^2 driven by a programmable power supply HCS-3300. Temperature of the heaters and LN crystals was measured by FLIR 7 Infrared Thermal Imaging Camera.

The contact wire and metal sheet: Equalization of potentials of the liquid meniscus and the underside of the LN crystal significantly increases the electric field strength near the meniscus. Moreover, it helps to compensate the excess of charge accumulating in the liquid sample during the emission of the charged droplets. To this end, we introduced a contact wire electrically connecting the meniscus and a thin metal sheet on the underside of the LN crystal. The contact wire and metal sheet were made of the same 0.05 mm copper foil that covers the surface of the Peltier element and was cut 1 mm wide and 30 mm long to form the wire (in fact, any conductive material can be used for this purpose).

Electric field simulation: Finite element method was used for simulation of electric field generated around LN crystal and particularly in the gap between the crystal and the fluid meniscus. Electrostatic model of PDA is described below. LN crystal is represented as a square dielectric plate with the dielectric constant ε=28.5. The plate is enclosed within a bounding box with dimensions of 160x160x100 mm^3 and with zero potential on its boundaries. Note that to choose the dimensions of that box, there is a trade-off between a stray capacitance introduced by the box and the memory and time usage during the simulation. In order to

decrease the memory and time consumption, the model volume is reduced by a quarter using the symmetry boundaries at *ZX* and *ZY* planes which are perpendicular to the LN plate and pass through its geometrical centre (see Figure 1a). Electric displacement *D* is set at the LN crystal surfaces which are perpendicular to the *Z* axis to describe polarization of the crystal caused by thermal stimulation which is assumed homogeneous. The electric displacement value is defined by the formula $D = \sigma$, where $\sigma = p\,\Delta T$ is a surface charge density generated on the opposite crystal surface by a temperature variation ΔT. The value p=-8.3 × 10^{-5} C m^{-2} K^{-1} is assumed for the LN pyroelectric coefficient.

Measurement of a surface electric potential of thermo-stimulated LN crystal plates: Surface electric potential of LN crystal stimulated by Linkam heater was measured by two kinds of electrostatic voltmeters: Monroe Isoprobe Model 244A and TREK Model 341A for potential up to 3 kV and up to 20 kV, respectively. LN crystal was placed upon the heater as it is shown in Figure 3a. The "ground" electrode of the voltmeter was connected to the heater disk and the probe electrode was placed at the distance of about 1.5 mm over the geometrical centre of the upper surface of the LN plate.

Optical recording of droplets accumulation: A side view of fluid dispensing was recorded by optical set-up consisted of a collimated blue LED M470L3-C1, 10× objective Mitutoyo BD Plan Apo, and camera CS2100M-USB with frame rate of 50 fps purchased from Thorlabs, Inc. After being processed by ImageJ® program, the image data were analysed using MATLAB®.

Supporting Information
Supporting Information is available from the Wiley Online Library or from the author.

References

[1] M. Cuendet, A. D. Mesecar, D. L. DeWitt, J. M. Pezzuto, *Nat. Protoc.* **2006**, *1*, 1915.

[2] J. L. Arlett, E. B. Myers, M. L. Roukes, *Nat. Nanotechnol.* **2011**, *6*, 203.

[3] M. S. Albert, S.T. DeKosky, D. Dickson, B. Dubois, H. H. Feldman, N.C. Fox, A. Gamst, D. M. Holtzman, W. J. Jagust, R. C. Petersen, P. J. Snyder, M. C. Carrillo, B. Thies, C. H. Phelps, *Alzheimers Dement*. **2011**, *7*, 270.

[4] H. S. Huang, C. L. Tsai, J. Chang, T. C. Hsu, S. Lin, C. C. Lee, *Clin. Microbiol. Infect.* **2018**, *24*, 1055.

[5] B. C. Giordano, D. S. Burgi, S. J. Harta, A. Terraya, *Anal. Chim. Acta* **2012**, *718*, 11.

[6] M. R. G. Kopp, M. Linsenmeier, B. Hettich, S. Prantl, S. Stavrakis, J.-C. Leroux, P. Arosio, *Anal. Chem.* **2020**, *92*, 5803.

[7] R. Kwak, S. J. Kim, J. Han, *Anal. Chem.* **2011**, *83*, 7348.

[8] D. T. Phan, Y. Chun, N.-T. Nguyen, *RSC Adv.* **2015**, *5*, 44336.

[9] F. Gentile, G. Das, M. L. Coluccio, F. Mecarini, A. Accardo, L. Tirinato, R. Tallerico, G. Cojoc, C. Liberale, P. Candeloro, P. Decuzzi, F. De Angelis, E. Di Fabrizio, *Microelectronic Engineering* **2010**, *87*, 798.

[10] A. Zhizhchenko, O. Vitrik, S. Syubaev, A. Kuchmizhak, in *AIP Conference Proceedings 1874*, **2017**, 040061.

[11] J. R. Trantum, M. L. Baglia, Z. E. Eagleton, R. L. Mernaugh, F. R. Haselton, *Lab Chip* **2014**, *14*, 315.

[12] P. Ferraro, S. Coppola, S. Grilli, M. Paturzo, V. Vespini, *Nat. Nanotechnol.* **2010**, *5*, 429.

[13] S. Coppola, V. Vespini, S. Grilli, P. Ferraro, *Lab Chip* **2011**, *11*, 3294.

[14] V. Vespini, S. Coppola, S. Grilli, M. Paturzo, P. Ferraro, *Lab Chip* **2011**, *11*, 3148.

[15] O. Gennari, L. Battista, B. Silva, S. Grilli, L. Miccio, V. Vespini, S. Coppola, P. Orlando, L.

Aprin, P. Slangen, P. Ferraro, *Appl. Phys. Lett.* **2015**, *106*, 054103.

[16] S. Grilli, L. Miccio, O. Gennari, S. Coppola, V. Vespini, L. Battista, P. Orlando, P. Ferraro, *Nat. Commun.* **2014**, *5*, 5314.

[17] R. Rega, M. Mugnano, E. Oleandro, V. Tkachenko, D. del Giudice, G. Bagnato, P. Ferraro, S. Grilli, S. Gangemi, *Sensors* **2020**, *20*, 3567.

[18] R. Rega, J. F. Muñoz Martinez, M. Mugnano, E. Oleandro, O. Gennari, P. Orlando, G. Cabassi, V. Pelizzola, P. Ferraro, S. Grilli, in *Proc. SPIE 11060, Optical Methods for Inspection, Characterization, and Imaging of Biomaterials IV*, **2019**, 1106009.

[19] R. Rega, M. Mugnano, D. del Giudice, S. Itri, V. Tkachenko, V. Vespini, S. Coppola, E. Mazzon, E. Oleandro, P. Ferraro, S. Grilli, in *Proc. SPIE 11361, Biophotonics in Point-of-Care*, **2020**, 113610N.

[20] F. J. Higuera, S. E. Ibanez, A. J. Hijano, I. G. Loscertales, *J. Aerosol Sci.*, **2013**, *66*, 193.

[21] S. V. Kalinin, Y. Kim, D. D. Fong, A. N. Morozovska, *Rep. Prog. Phys.*, **2018**, *81*, 036502.

[22] M. N. Horenstein, *J. Electrostat.*, **1995**, *35*, 203.

[23] G. Rosenman, D. Shur, Ya. E. Krasik, A. Dunaevsky, *J. Appl. Phys.*, **2000**, *88*, 6109.

[24] A. J. Hijano, I. G. Loscertales, S. E. Ibànez, F.J. Higuera, *Phys. Rev. E*, **2015**, *91*, 013011.